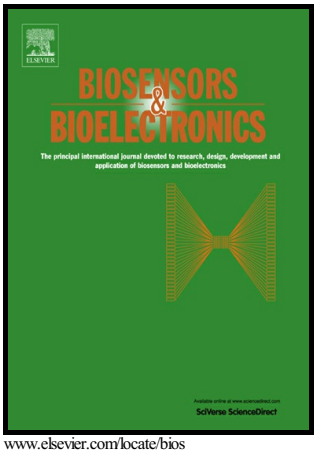

www.elsevier.com/locate/bios

Direct detection of cysteine using functionalized $BaTiO_3$ nanoparticles film based self-powered biosensor

Sophia Selvarajan, Nagamalleswara Rao Alluri, Arunkumar Chandrasekhar, Sang-Jae Kim

PII: S0956-5663(16)31234-9
DOI: http://dx.doi.org/10.1016/j.bios.2016.12.006
Reference: BIOS9399

To appear in: *Biosensors and Bioelectronic*

Received date: 9 September 2016
Revised date: 1 December 2016
Accepted date: 2 December 2016

Cite this article as: Sophia Selvarajan, Nagamalleswara Rao Alluri, Arunkuma Chandrasekhar and Sang-Jae Kim, Direct detection of cysteine usin functionalized $BaTiO_3$ nanoparticles film based self-powered biosenso *Biosensors and Bioelectronic,* http://dx.doi.org/10.1016/j.bios.2016.12.006

Direct detection of cysteine using functionalized $BaTiO_3$ nanoparticles film based self-powered biosensor

Sophia Selvarajan[a], *Nagamalleswara Rao Alluri* [b], *Arunkumar Chandrasekhar* [c], *Sang-Jae Kim*[a,c,*]

[a]Nanomaterials and System Lab, Department of Advanced Convergence Technology and Science, Jeju National University, Jeju 690-756, Republic of Korea

[b]Nanomaterials and System Lab, Department of Mechanical Engineering, Jeju National University, Jeju 690-756, Republic of Korea

[c]Nanomaterials and System Lab, Department of Mechatronics Engineering, , Jeju National University, Jeju 690-756, Republic of Korea

[*]*Corresponding Author*

Prof. Sang-Jae Kim,

Fax: 0082-64-756-3886; Tel: 0082–64-754-3715.

E-mail: kimsangj@jejunu.ac.kr

Postal address:

D130, Nano Materials & System Lab

Engineering Building-4,

Jeju National University,

Ara-1-dong, Jeju-si, Jeju-do,

Republic of Korea, 690-756

Abstract

Simple, novel, and direct detection of clinically important biomolecules have continuous demand among scientific community as well as in market. Here, we report the first direct detection and facile fabrication of a cysteine-responsive, film-based, self-powered device. NH_2 functionalized $BaTiO_3$ nanoparticles (BT-NH_2 NPs) suspended in a three-dimensional matrix of an agarose (Ag) film, were used for cysteine detection. $BaTiO_3$ nanoparticles (BT NPs) semiconducting as well as piezoelectric properties were harnessed in this study. The changes in surface charge properties of the film with respect to cysteine concentrations were determined using a current–voltage (*I*-*V*) technique. The current response increased with cysteine concentration (linear concentration range = 10 µM to 1 mM). Based on the properties of the composite (BT/Ag), we created a self-powered cysteine sensor in which the output voltage from a piezoelectric nanogenerator was used to drive the sensor. The potential drop across the sensor was measured as a function of cysteine concentrations. Real-time analysis of sensor performance was carried out on urine samples by non-invasive method. This novel sensor demonstrated good selectivity, linear concentration range and detection limit of 10 µM; acceptable for routine analysis.

Keywords: NH_2-functionalized $BaTiO_3$ NPs; agarose 3D matrix; self-powered cysteine bio-sensor; *I*–*V* technique; piezoelectric nanogenerator; non-invasive (urine)

1. Introduction

Cysteine, an essential amino acid containing a thiol group, has vital roles in homeostasis and as a precursor; it has also been used as a biomarker (Jung et al., 2012a). Deviations in cysteine concentration from physiological levels (30–200 μM) has been linked to chronic diseases, such as rheumatoid arthritis, Parkinson's disease, Alzheimer's disease, and even adverse pregnancy outcomes (Jung et al., 2012b)(Yang et al., 2016)(Gong et al., 2015)(Zhang et al., 2007). Thus, a facile, direct method for cysteine detection could have considerable significance, given the currently available approaches, such as those based on high-performance liquid chromatography (Nekrassova et al., 2003), colourimetric and fluorescence spectroscopy (Jung et al., 2012b), capillary electrophoresis, and electrochemical voltammetry (Park et al., 2014). The existing methods have certain drawbacks such as complex sample preparation before measurement, time-consuming processes, and the need for sophisticated instrumentation. With this in mind, there is a continuing need for the development of a simple and rapid sensor capable of identifying cysteine in routine analysis.

One possible approach is a stimulus-responsive nanodevice; these devices have gained much attention among researchers due to their vital applications in theranostics, biomolecule detection (Sun et al., 2014), and drug delivery (Xia et al., 2007), avoiding off-target effects and false-positive results. A promising route to a stimulus-responsive system involves nanocomposites, comprising nanoparticles and polymers. Nanocomposites have been used in diverse applications in bio-sensing, electronics, drug delivery, nano-medicine, and catalysis (Thoniyot et al., 2015) due to their enhanced functionality. Typically, the polymer plays the role of a matrix (substrate) and functionalized nanoparticles (NPs) are involved in sensing the target molecule. In this study, an agarose (Ag) biopolymer was used as the substrate and amine-functionalised $BaTiO_3$ NPs (BT-NH_2 NPs) were used for the selective detection of cysteine for the first time. Agarose, a polysaccharide consisting of

alternating residues of α-1,3-linked D-galactose and R-1,4-linked 3,6-anhydro-R-L-galactopyranose, forms left-handed helices as a linear polymer. These helices aggregate into long fibres, which, in turn, associate in three dimensions to form a three-dimensional (3D) gel network (Horger et al., 2009). Agarose has considerable chemical, thermal, and physical stability and is less likely to interact with biomolecules, making it a preferred matrix for use with protein and nucleic acids. Agarose films have higher stiffness than poly(vinylidene fluoride) films due to inter- and intra-hydrogen bonding of its functional groups. Also, the unique chemical functionality of agarose has prompted its use as an alternate electrode material and multifunctional green battery material (Hwang et al., 2016).

The $BaTiO_3$ (BT) nanoparticles used here are a well-known metal oxide with an ABO_3 perovskite structure, having (n-type) semiconducting (Selvarajan et al., 2016) and inherent piezoelectric properties (Park et al., 2012). Its unique features, such as biocompatibility, second-harmonic generation (SHG) (Hsieh et al., 2010), low dielectric constant, and high piezoelectric coefficient, make it a potential candidate for applications in biosensing (Selvarajan et al., 2016), theranostics (FarrokhTakin et al., 2013), bioimaging (Ĉulić-Viskota et al., 2012), and piezoelectric-based energy harvesting (Alluri et al., 2015). Furthermore, such ceramic perovskite-structured metal oxides have applications in electrical and electronic devices. As yet, the fact that this has still not been exploited extensively for biological applications renders great interest for self-powered biosensing and theranostic applications. Self-powered systems with novel features, such as battery-less operation, portability, point-of-care diagnosis, and implantable applications (Yu et al., 2013), can be developed using piezoelectric nanogenerators (PNG), a relatively old energy-harvesting technology in which mechanical energy is converted into electrical energy. Self-powered nanosensors combine the nanogenerator with a sensor, through internal or external integration. Thus, the energy harvested from the nanogenerator is used to drive the sensor.

Based on the novel approaches mentioned above, in the present work, a self-powered cysteine sensor was demonstrated by externally integrating a cysteine sensor with a PNG. Ag/BT-NH_2 film-based cysteine sensor with metal–semiconductor–metal (MSM) configuration was connected in parallel to a BT/Ag film-based piezoelectric nanogenerator (BT/Ag PNG). The cysteine sensor's analytical outputs were analysed using a current–voltage (*I–V*) technique. In a self-powered cysteine sensor, the voltage across the sensor decreases with an increase in the cysteine concentration; this potential drop is measured as the sensing signal, in accordance with *I–V* studies. To our knowledge, this is the first report of a self-powered cysteine sensor based on a direct detection technique and BT NPs. The as-fabricated sensor demonstrated comparable or enhanced performance, compared with conventional sensors. The novelty in our work stems from the direct, self-powered detection method using functionalized BT NPs, harnessing both its semiconducting and piezoelectric properties. The proposed sensor can be developed as a possible prototype for implantable and point-of-care diagnostic devices in the near future.

2. Experimental section

2.1. Synthesis of BT NPs

Pristine, tetragonal-phase BT NPs were synthesised via a conventional solid-state reaction method. The high-purity precursors $BaCO_3$ (99.95%, High Purity Chemicals) and TiO_2 (98%, Daejung Chemicals) were taken according to the atomic ratio of $BaTiO_3$ and mixed well using a pestle and mortar in acetone for 30 min until a homogeneous powder was obtained. It was then placed inside a alumina combustion boat and heated to 1200°C for 2 h in an open-tube furnace at a heating rate of 2.5°C/min (Selvarajan et al., 2016). The final product was taken out of the furnace after the reaction was complete and cooled naturally. The as-

synthesised NPs' phase and surface morphology were confirmed by Raman spectroscopy, X-ray diffraction (XRD), and field-emission scanning electron microscopy (FE-SEM) analyses.

2.2. NH_2 functionalization of BT NPs

The BT NPs obtained were functionalized with NH_2. A two-step process was used whereby the BT NPs were first functionalized with OH groups and then with NH_2 groups via (3-aminopropyl) triethoxysilane (APTES) treatment (Ĉulić-Viskota et al., 2012) (FarrokhTakin et al., 2013). First, 120 mg of BT NPs were treated with 1M nitric acid for 2 h and then washed until neutral pH was attained. They were further treated with H_2O_2 overnight and centrifuged (5000 rpm, 5 min). To the hydroxylated BT (BT-OH) NP product, 140 µL of APTES, 250 µL ammonium solution, and 36 mL of anhydrous ethanol were added and treated at 70°C for 8 h. After cooling, the sample was washed three times with ethanol to remove unwanted reactants. The resulting BT-NH_2 nanoparticles were dried and stored in a vacuum environment. NH_2 functionalization of the BT surface reduced aggregation of the NPs, resulting in a more dispersed solution (Culic-viskota, 2012).

2.3. Fabrication of the cysteine sensor

A schematic diagram of the Ag/BT-NH_2 film-based cysteine sensor is provided in Fig. 1A. The fabrication protocol is facile and straightforward, requiring no sophisticated equipment or process. The film was fabricated through a simple solution-casting technique. Specifically 0.2% (w/v) of BT-NH_2 NPs were dispersed in 1% predissolved agarose (Ag was dissolved in twice-distilled water in a microwave oven for 1 min) and allowed to gel *in situ* after casting the composite solution in Petri dishes. The film was then dried at 45°C for 24 h and later sliced according to the device dimensions (0.5 × 1 cm). Polyethylene terephthalate was used as the substrate on to which the film was attached. Electrical contacts were established using

silver paste, and external connections were made using copper wires. An epoxy layer was used to cover the electrodes to prevent possible contact between the electrodes and buffer solution.

2.4. Fabrication of the BT/Ag PNG

Fabrication of the BT/Ag PNG involved three simple steps: composite film formation, establishment of electrodes and external connections, and finally device packaging, as shown in Fig. 1B. The BT/Ag film was formed by a simple solution-casting technique as described for the fabrication of the sensor. Specifically 0.1, 0.2, and 0.4 % (w/v) BT NPs in 1% Ag were used for composite film fabrication and 1% Ag for pure Ag film fabrication. To the as-fabricated composite film (3 × 3 cm), Al foil-based electrodes were attached on the top and bottom; electrical contacts were made using silver paste. External connections were established using copper wires. The device was finally packed with a polydimethylsiloxane stamp to protect it from external factors, such as humidity and temperature.

2.5. Instrumentation

An X-ray diffractometer (XRD, Rigaku), operating at 40 kV/10 mA using Cu Kα radiation (2θ range, 20–80°) at room temperature, was used to confirm the crystalline phase formation in the BT NPs and composite films. Raman spectra for all samples were recorded from 100 to 3000 cm^{-1} with an excitation source of 514 nm, using a high-throughput, single-stage spectrometer (Lab RAM HR Evaluation, Japan). The surface morphology of all samples was characterised using FE-SEM (JEOL, JSM-6700F). A Prizmatiz multi-wavelength light-emitting diode (LED) light source was used as the ultraviolet (UV) source (365 nm). *I–V* measurements were made using a Frequency Variable CV-IV System (B 1500A). The open circuit voltage (V_{oc}) and short circuit current (I_{sc}) of the PNG were recorded with a

nanovoltmeter (Keithley 2182A) and a picoammeter (Keithley 6485), respectively. The PNG output was measured by triggering with a mechanical load of 2 N.

3. Results and Discussion

3.1. Structural characterisation

The successful NH_2 functionalization of BT NPs using APTES (a silane coupling agent) was confirmed through Fourier-transform infrared (FTIR) analysis. The corresponding FTIR spectra of BT NPs before and after surface modification are shown in Fig. 1C. The BT NP's characteristic Ti-O stretch can be observed at 550 cm^{-1}. Prior to amine functionalization, BT NPs were hydroxylated, which was confirmed by −OH stretching and vibrational modes at 3450 cm^{-1} and 1650 cm^{-1}. The peak around 1430 cm^{-1}, indicating the adsorbed carbonate group, was eliminated after surface hydroxylation. The Si-CH_3 stretch at around 800 cm^{-1} and the double overlapping peak between 1000 and 1200 cm^{-1} corresponding to the Si-O-Si bond, indicates appropriate silane coating of the BT NPs (Ĉulić-Viskota et al., 2012). Primary amine bending at 1550 cm^{-1} and the alkane group stretching vibrational mode at 2960 cm^{-1} further confirmed the successful surface modification of BT NPs using APTES (Coates et al., 2000).

The phases of individual components and the composites were determined using Raman and XRD characterisation. Pristine BT NPs and BT-NH_2 NPs have tetragonal phases. No change in phase was observed, even after composite film formation (Ag-BT-NH_2), as shown in the XRD spectrum (Fig. 1D). The diffraction peak splitting at 45° (200/002), observed with BT, BT-NH_2, and Ag/BT-NH_2 film demonstrated the tetragonal nature of BT NPs, consistent with the reference ICDD 98-001-3771 pattern (Alluri et al., 2015). In the case of the agarose film, the peak at ~19° illustrates a high degree of crystallinity (Freile-Pelegrin et al., 2007). Moreover, the characteristic peaks at 305 cm^{-1} and 518 cm^{-1} in the Raman

spectrum (Fig. S1A) confirmed the tetragonality of BT NPs, indicating the presence of Ti^{4+} ions in the parent lattice; the peaks were assigned to A1 and B1 modes, respectively (Hayashi et al., 2013).

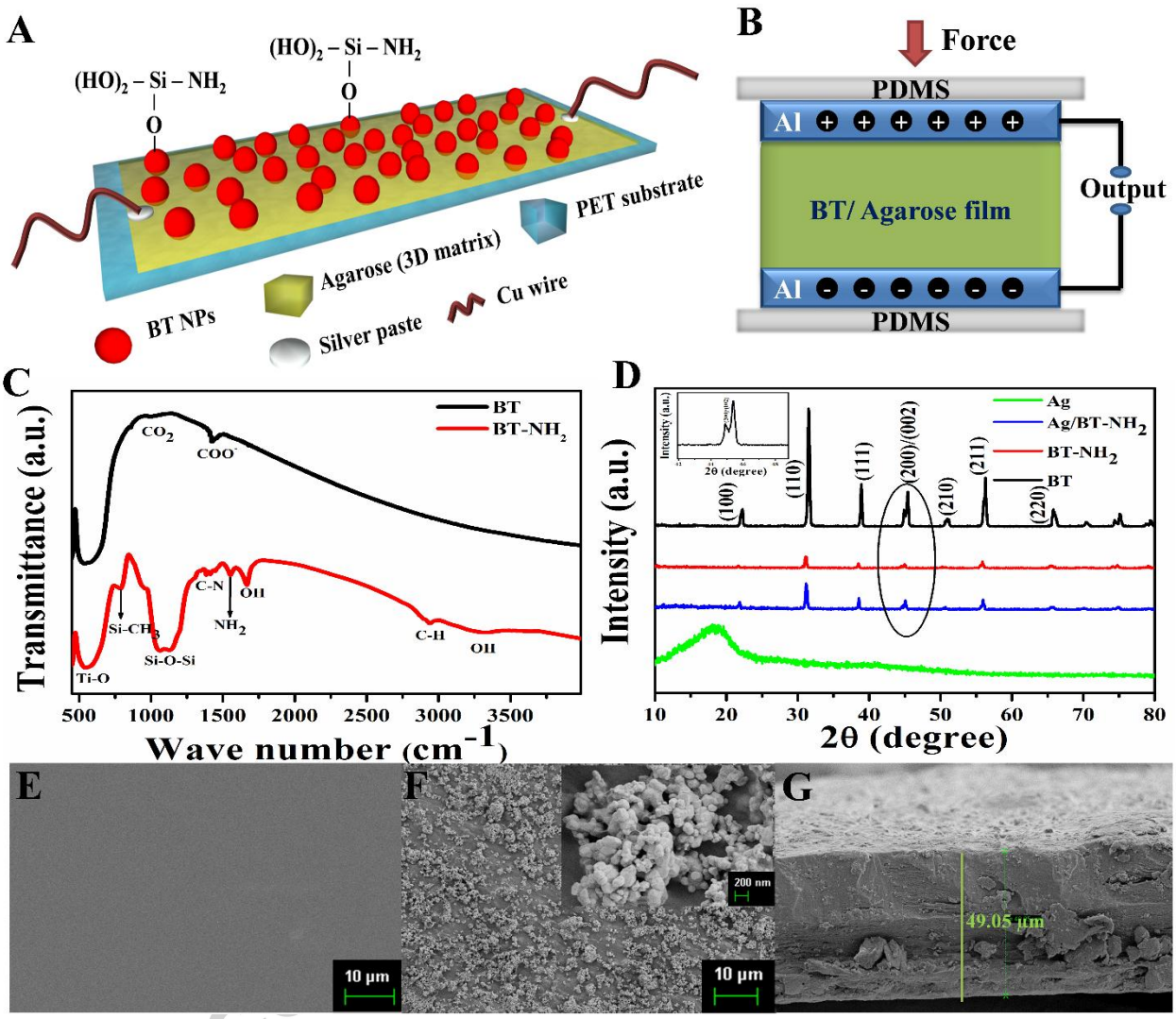

Figure 1.

The surface morphology of individual components and the composites were analysed through FE-SEM characterisation. As-synthesised BT NPs have random shapes with size ≤ 200 nm (Fig. S2A). The low-magnification SEM image in Fig. 1E shows that pure agarose film has a smooth surface in the top view. Because gelation of agarose occurred in the presence of BT-NH_2 NPs, the NPs are in intimate contact with the polymer matrix, being embedded within the densely packed microstructure of the agarose matrix, as confirmed by

SEM images (Fig. 1F: the inset shows BT-NH_2 NPs of ≤ 200 nm, and Fig. S2B-C). The cross-sectional view of the Ag/BT-NH_2 film showed a uniform film thickness of ~50 µm (Fig. 1G). Possible interactions between NPs and the agarose polymer could be mediated through hydrogen bonding or electrostatic interactions, resulting in intimate contact between them (Wang et al., 2010). Thus, the agarose matrix served as a supporting medium (binder) for the BT-NH_2 NPs and connected them to the current collector (electrodes) (Hwang et al., 2016).

3.2. Device characterisation and investigation of its sensing feasibility

To confirm the sensing feasibility of the Ag/BT NPs film, the surface charge properties of the film were examined with respect to pH (range: 3–7) using *I–V* technique (Sun et al., 2014). Figure S3A shows that for the Ag/BT NP film-based device, the change in pH from 7 to 3 resulted in an increase in current at −1 V from −50 µA to −175 µA, respectively. In contrast, for the Ag film alone (Fig S3B), the increase in current was negligible (−0.5 µA to −4.5 µA) at −1 V. This confirmed that the agarose served as a matrix for the suspended BT NPs and that it does not make a significant contribution to sensing.

We also investigated the effect of BT-NH_2 NP concentration and UV light exposure in cysteine detection. To confirm whether UV light could catalyse the reaction, the Ag/BT-NH_2 film-based sensor was irradiated with a UV source (365 nm) after the addition of cysteine at different concentrations (Fig. S4A). As a control, the experiment was carried out under the same conditions with no UV irradiation (Fig. S4B). UV irradiation catalysed the reaction and enhanced the output, showing more than a two-fold increase (relative current at −4 V; $I\text{-}I_0/I_0$) versus the control (see the 2D graph in Fig. 2A). Thus, the 365-nm UV source was used in subsequent experiments.

The effect of BT-NH_2 NP concentration in cysteine detection was studied by comparing two concentrations of BT-NH_2 NPs (0.1 and 0.2% w/v), as shown in Fig. S5. The output current increased (relative current at −4 V) with BT-NH_2 NP concentration, as shown in the 3D graph in Fig. 2B. From this, 0.2% w/v of BT-NH_2 NPs was taken to be the optimum concentration, as the output current obtained was sufficient for cysteine detection.

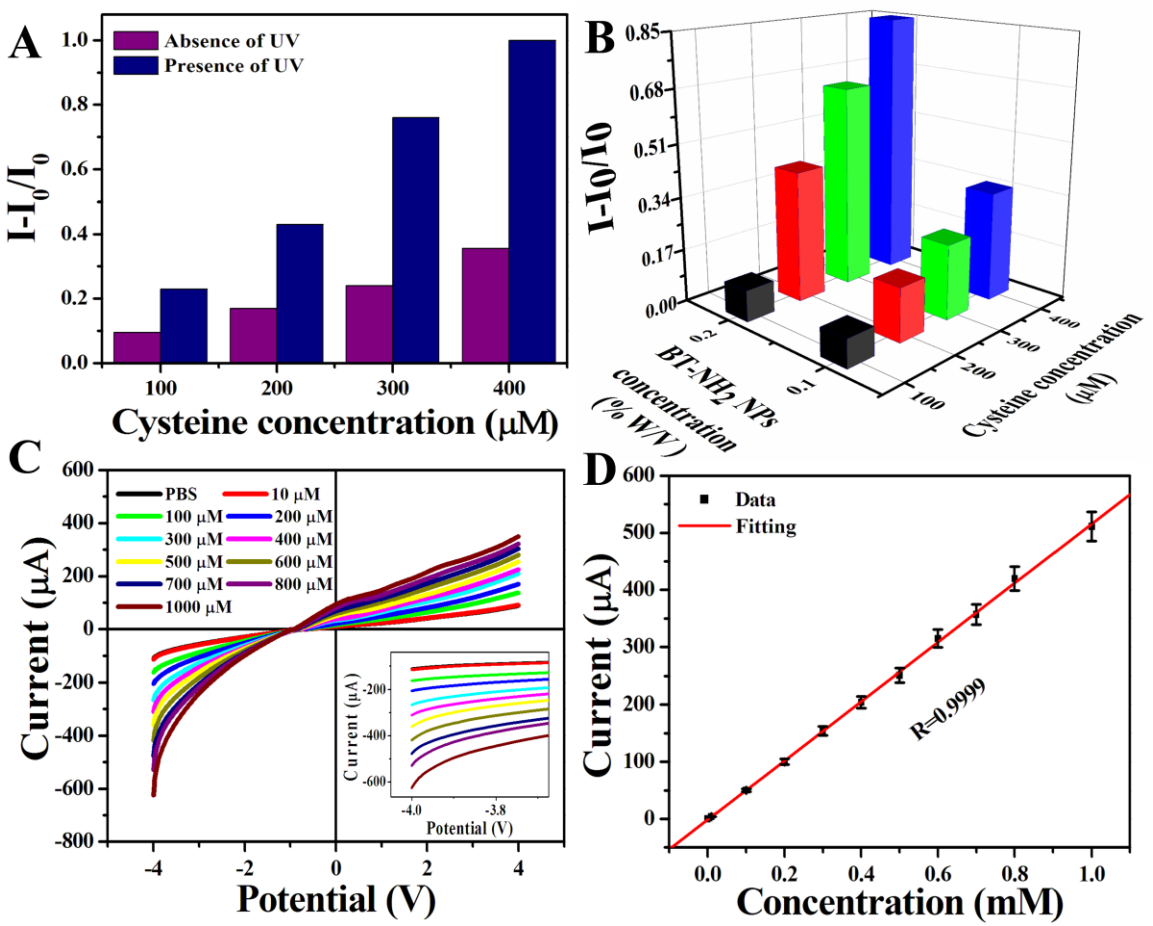

Figure 2.

3.3. Cysteine detection by an I–V technique

The cysteine response of the Ag/BT-NH_2 film-based sensor was determined using an *I–V* technique. *I–V* curves were measured over a potential range of −4 to +4 V in phosphate buffer solution (0.1 M PBS; pH 7) containing various cysteine concentrations (10 µM to 1mM), as shown in Fig. 2C. The inset of the figure shows an enlarged portion at −4 V. The device current output was normalised (saturated) with PBS before taking measurements with different concentrations of cysteine. After the Ag/BT-NH_2 film-based sensor was exposed to UV light (365 nm) for 15 min in the presence of 10 µM cysteine, there was an increase in the current output at −4 V. Furthermore, with an increase in cysteine concentrations (10 µM to 1 mM), the current at −4 V increased. This increase in current showed a linear relationship with cysteine concentrations (correlation coefficient: 0.9999), as in the calibration curve (Fig. 2D). The limit of detection (LOD) was ~10 µM; LOD was calculated from the calibration curve by the "3s/m" criteria, where s is the standard deviation and m is the slope of the calibration curve. With physiological levels of cysteine of the order of 30–200 µM (Jung et al., 2012a), the as-fabricated sensor with a sensitivity of ~506 µA/mM should be sufficient for practical, routine analysis. As a control, the experiment was also performed using only PBS to ensure that the current signal obtained was due to cysteine and was not from ions present in the PBS (electrolyte), as shown in Fig. S6A-B. From Fig. S6C, it can be seen that with an increase in the PBS concentration, there was no significant increase in current output at −4 V, compared with the current change ratio in the presence of cysteine (100 to 400 µM). The Ag/BT-NH_2 film has a positive surface charge in the absence of cysteine under the given experimental conditions. A rapid increase in current occurred at −4 V upon addition of cysteine, as expected from the pI of cysteine (5.07), because it would be negatively charged at the given pH of our experimental conditions, leading to the binding of negatively charged species to the film and the depletion of positively charged species (Sun et al., 2014). With an increase in

cysteine concentration, the negative charge on the film surface increased, resulting in a significant increase in current at −4 V.

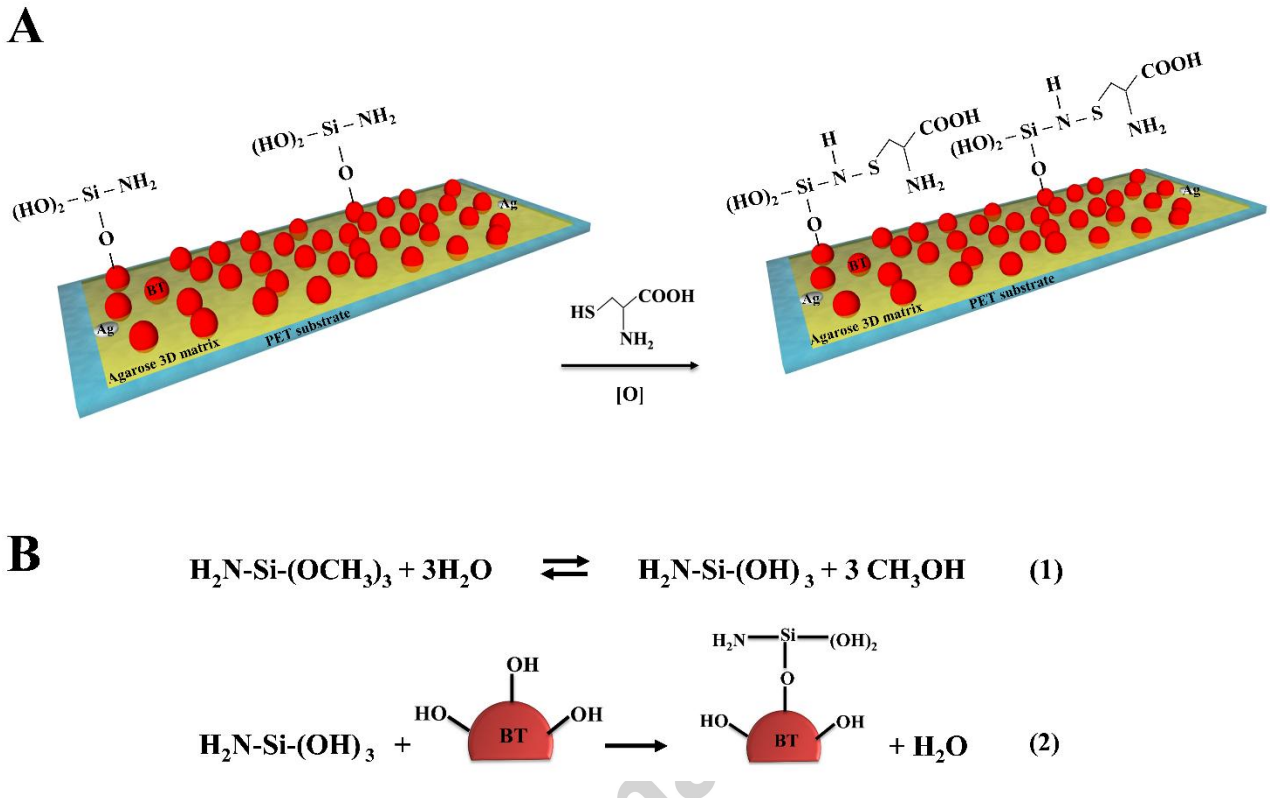

Figure 3.

3.4. Proposed working mechanism of the Ag/BT-NH_2 film-based cysteine sensor

An increase in negatively charged species (cysteine) on the film will increase the charge carrier density (electrons) and thus eventually decrease the resistance across the film, leading to an increased output current (Selvarajan et al., 2016). This typical MSM device behaviour was observed in the *I–V* data (Selvarajan et al., 2016) (Yu et al., 2013). In absence of buffer or cysteine, Ohmic behaviour was observed (Fig. S1A-B); with the introduction of different concentrations of cysteine, the *I–V* curves became non-linear (Fig. 2C). The increase in charge carrier density (electrons) in the film lowers the Schottky barrier height on the drain side (M-S interface), resulting in a significant increase in the output current of the Ag/BT-NH_2 film-based sensor.

A possible response mechanism can be explained as follows. R-SH (thiol) in the presence of BT-NH_2 (positive residue) loses a H^+ ion and becomes a thiolate (Carroll, 2012). The thiolate side chain ($R\text{-}S^-$) in cysteine is a strong nucleophile (Jung et al., 2012a) and acts as a Lewis base, ready to react with the NH_2 group on BT NPs (electrophiles). This results in a nucleophilic attack of $R\text{-}S^-$ on the NH_2 group, leading to S-N bond formation (sulfenamides; Fig. 3A; equation (1)) (Johnson et al., 1970). Thus, cysteine binds to the film, increasing its surface negative charge. A detailed reaction scheme for the functionalization of BT NPs with amine groups is provided in Fig. 3B. The proposed sensor's analytical throughput (LOD and linear concentration range) is better than or comparable to existing cysteine sensors (Table 1). These reported sensors are based on colourimetric, amperometric, and fluorescence-based techniques, whereas the sensor developed is self-powered and based on a direct detection technique. Thus, our novel sensor design provides efficient cysteine detection with minimal sample processing and time consumption; as such, being a prototype for implantable and point-of-care diagnostic devices.

$$RS^- + H_2N - R' \rightarrow RSNR' + H_2O \quad (1)$$

3.5. Real-time analysis and interference studies

The sensor was further assessed with complex matrices like urine samples for real-time detection. Non-invasive detection using urine samples has great advantages, such as patient compliance and ease of sample handling. An abnormal level of cysteine in urine is a result of a disorder or disease (Sun et al., 2014). The physiological level of cysteine in urine mirrors changes in plasma, where the level varies from 30 to 200 µM (Refsum et al., 1986) (Kaniowska et al., 1998). Thus, for real sample analyses, the concentration range studied was 10–500 µM, which covers the physiological range of cysteine. The urine samples collected were diluted by a factor of 10 with 0.1 M PBS (pH 7) and immediately used for analysis. The diluted samples were spiked with known concentrations of cysteine (10-500 µM). *I–V* curves

of the Ag/BT-NH_2 film-based cysteine sensor in response to different concentrations of cysteine-spiked urine samples are shown in Fig. 4A (inset shows the enlarged portion at −4 V). The *I–V* characteristics obtained were consistent with the cysteine concentrations (10 µM to 1 mM) shown in Fig. 2C. From the calibration plot obtained (Fig. 4B), there was a linear relationship between the current obtained at −4 V and the cysteine concentration (correlation coefficient: 0.9999) and LOD obtained was ~10 µM (3s/m criteria) which is in agreement with Fig. 2D. Thus the sensor is applicable for screening samples to check whether the cysteine level lies within the normal physiological range or not.

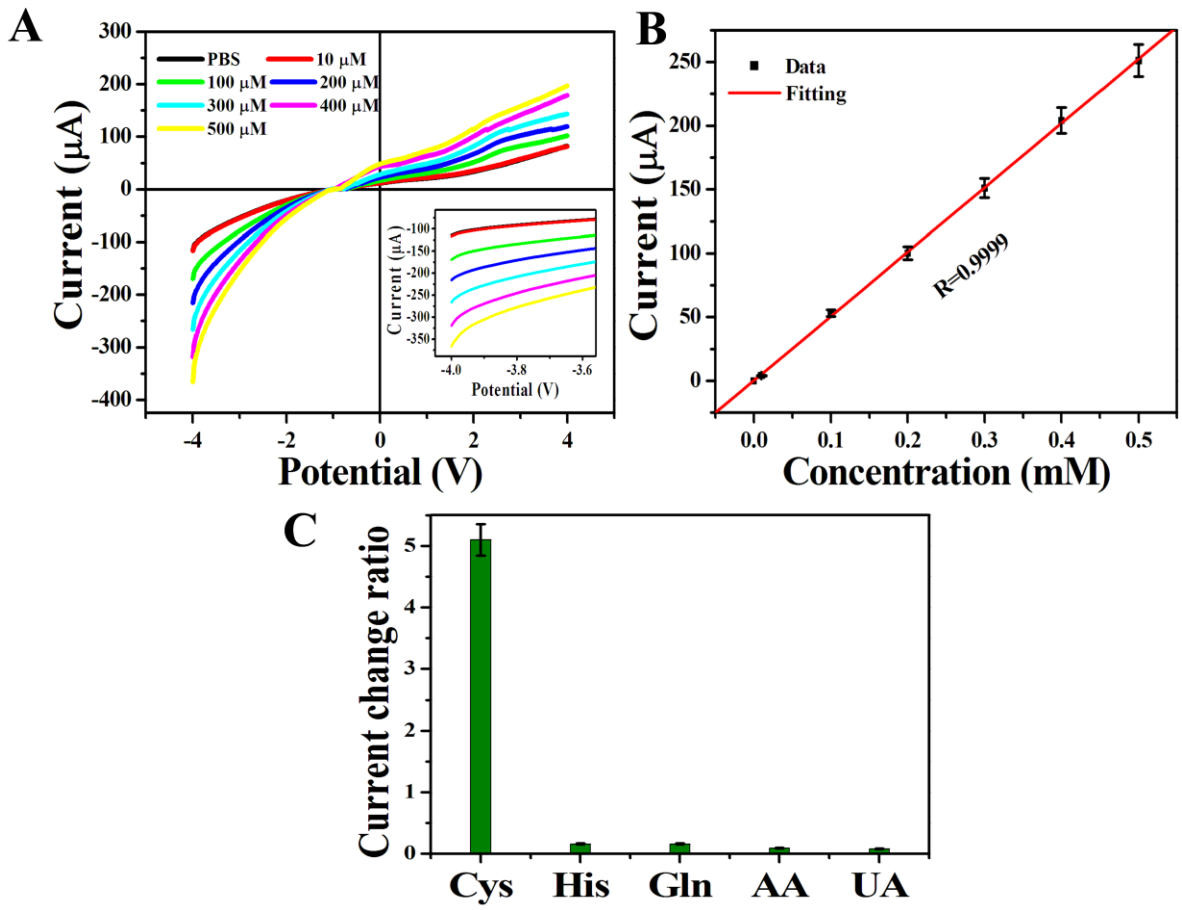

Figure 4.

The sensor has good selectivity towards cysteine compared to various interfering species, such as histidine (His), glutamine (Gln), ascorbic acid (AA), and uric acid (UA). The *I–V* curves of a Ag/BT-NH_2 film-based sensor in response to 1 mM concentrations of potentially

interfering species in the presence of PBS (electrolyte) are shown in Fig. S7A–D (the inset shows an enlarged portion at −4 V). There were negligible changes in current at −4 V, even at 1 mM concentrations of the interfering species. The current change ratios measured at −4 V in 0.1 M PBS (pH 7) with the addition of 1 mM Cys, His, Gln, AA, and UA are shown in Fig. 4C. From the negligible current change ratios for interfering species compared with that of cysteine, the sensor's selectivity towards cysteine is clear. Additionally, interference study for self-powered cysteine sensor was also performed using cysteamine; an aminothiol and a therapeutic drug used for treating cysteine related disorders (Fig. S8A–B). The open circuit potential drop across the sensor (peak-to-peak value) for 1 mM cysteamine is 65 V and to that of 1 mM cysteine is 1.5 V. Thus, the response of the sensor to cysteamine and cysteine is 18% and 98% respectively (~ 5.5 fold difference) as shown in Fig. S8B; once again confirms the sensor's selectivity. The experiments were repeated four times (denoted by error bars) and measurements were made over a time period of two months (stored at room temperature) which proves the sensors performance, reproducibility and stability.

3.6. Self-powered cysteine sensor

3.6.1. BT/Ag PNG

The novel approach to cysteine detection demonstrated prompted development of a self-powered sensor system. Agarose, a biopolymer, has been recently exploited in energy harvesting and storage devices, due to its unique chemical features (ether and hydroxyl groups) and properties, such as higher stiffness (due to inter- and intra-hydrogen bonding of its functional groups), as an electrode binder, multifunctional green battery material, and building element for battery separators (Hwang et al., 2016). A composite made of agarose and BT can be exploited to create a piezoelectric nanogenerator for energy harvesting, which can then be used as a power source for driving the Ag/BT-NH_2 film-based sensor. The

biopolymer agarose serves as a matrix for the BT NPs, assisting in film formation. BT/Ag PNGs of four different weight ratios (0, 0.1, 0.2, and 0.4% w/v), with 3 × 3 cm dimensions, were fabricated as described in the Experimental section. The V_{oc} and I_{sc} of these PNGs are shown in Fig. 5A and Fig. S9A-B. The 0.4% w/v BT/Ag PNG showed the best performance among the various weight ratios, with an average peak-to-peak V_{oc} of 80 V (Fig. 5B) and an average peak-to-peak I_{sc} of 285 nA (Fig. 5C) at a mechanical load of 2 N, the maximum values among the four weight ratios. With an increase in BT concentration, the nanogenerator's output voltage and current increased (Fig. 5A). The composite film with a higher % w/v of BT NPs showed higher performance compared with the pure Ag film and lower % w/v BT NPs. The piezoelectric potential generated from this device (0.4% w/v) can light up six commercial green LEDs (Fig. 5D), confirming its ability to power sensors and other low-power electronic gadgets. The as-fabricated PNG showed good stability, giving a stable output voltage of 80 V with no degradation, even for a period of 1000 s under a mechanical force of 2 N (Fig. 5E). Thus, this PNG was used as the power source to drive the as-fabricated cysteine sensor.

3.6.2. Working mechanism of PNG

The flexible PNG's mechanical energy is converted into electrical energy. When a compressive force is applied, orientation of dielectric poles in the BT/Ag composite film occurs, generating a piezoelectric potential. The perpendicular force acting on the composite film generates a piezopotential on both sides of the film, which, in turn, induces inductive charges on the top and bottom electrodes. The charge carriers create a potential difference, which drives electrons through the external circuitry (Saravanakumar et al., 2014). The V_{oc} and I_{sc} values of the PNG depends on the piezoelectric coefficient (d_{33}) (Selvarajan et al., 2016), given by

$$V_{OC} = \left(\frac{d_{33}}{K\epsilon_0}\right)\sigma Y t \quad (2)$$

$$I_{SC} = g_{33} K \epsilon_0 Y A \epsilon \quad (3)$$

where σ is the strain (perpendicular direction), Y is Young's modulus, T is the thickness of the device, K is the relative permittivity, ϵ_0 is the permittivity of free space, g_{33} is the piezoelectric voltage constant $\left(\frac{d_{33}}{K\epsilon_0}\right)$, ϵ is the applied strain, and A is the cross-sectional area of the device.

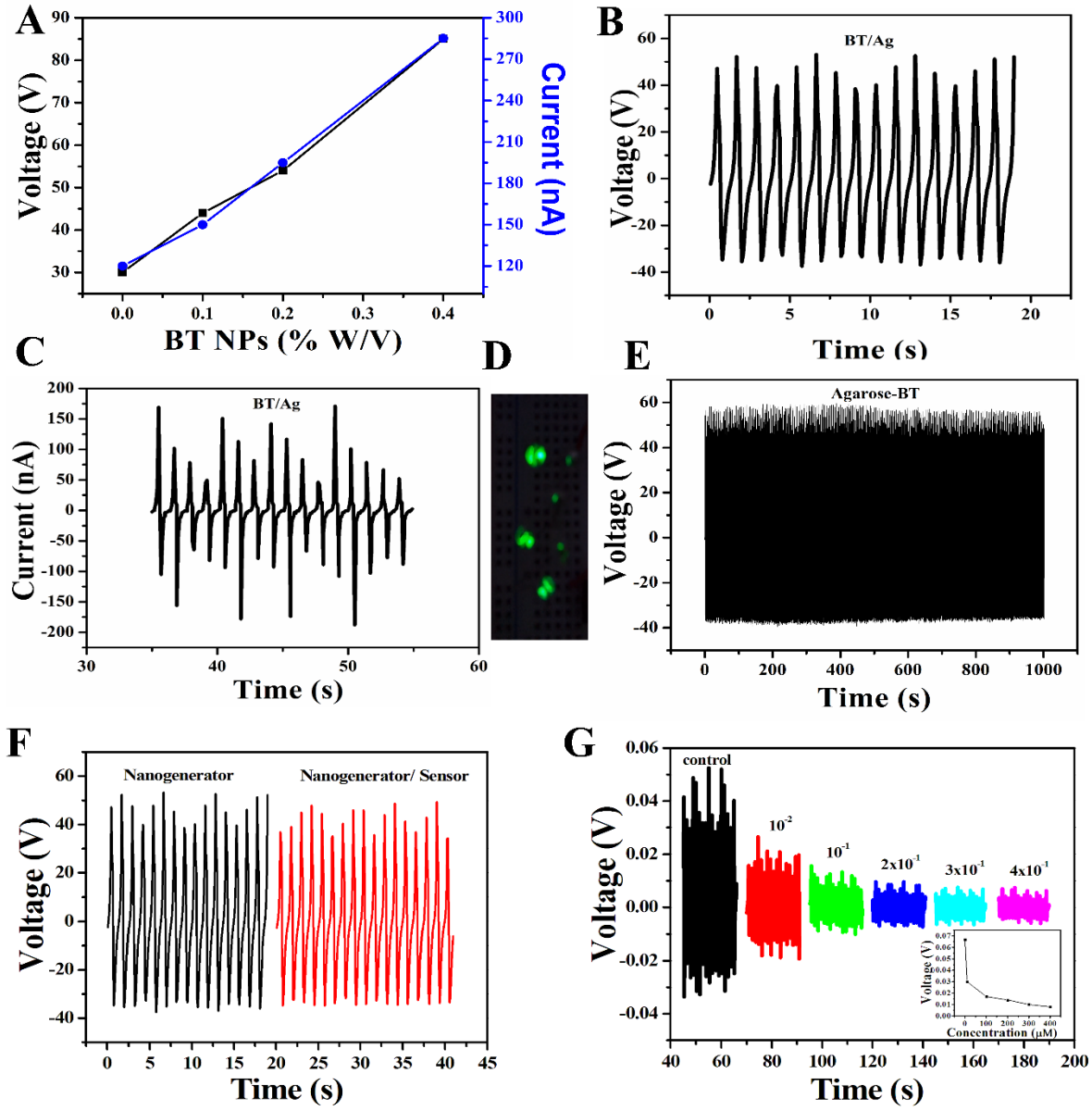

Figure 5.

Table 1. Comparison between cysteine sensors based on different detection techniques

Material employed	Detection technique	Limit of detection	Linear range concentration	Reference
Fluorescent AgAuNCs@11-MUA	Fluorometric	111 Nm	0.25-7 μM	(Sun et al., 2015)
GCE/MWCNTs/PEI/Au NPs electrode modified with DTNB	Amperometric	2.7 μM L^{-1}	9.0-250 μM L^{-1}	(Santhiago et al., 2010)
Coumarin derivative	Fluorometric	100 nM	0-0.9 mM	(Jung et al., 2012b)
Silver nanoparticles	Colourimetric	100 nM	0.1-1000 μM	(Han et al., 2014)
MIL-88A-derived Fe_3O_4-carbon Hierarchical nanocomposites	Amperometric	2 μM	0.007-14.18 mM	(Wang et al., 2015)
Tetraphenylethene-coumarin hybrid fluorophore	Fluorometric	5 μM	5-500 μM	(Lou et al., 2014)
NH_2-functionalised BT NPs suspended in agarose matrix	I–V technique	10 μM	10 μM-1 mM	This work
Tris(bipyridine)Ru(II) complex	Fluorometric	1.41 μM	15 to 180 μM	(Zhang et al., 2010)

In the case of a nanogenerator made of pure agarose film, the generation of electrical output is mainly from the functional groups (hydroxyl and ether) present in the agarose, causing inductive charges on the top and bottom Al electrodes. The difference in potential between the two electrodes drives the charge carriers through the external connections, leading to the generation of an electrical output. A PNG made from BT/Ag composite film showed better performance and thus was used for driving the sensor.

3.6.3. Integration of the cysteine sensor and BT/Ag PNG

The electrical output generated from the BT/Ag PNG was used to drive the Ag/BT-NH_2 film-based cysteine sensor. To demonstrate the self-powered device, the cysteine sensor was connected in parallel to the BT/Ag PNG. The PNG output and PNG/cysteine sensor (self-powered device) output (peak-to-peak V_{oc}: ~80 V @ 2 N, in the absence of buffer) was approximately the same, confirming that the sensor's resistance was equal to the PNG's resistance (1–50 MΩ; Fig. 5F). With the introduction of a buffer, the voltage across the sensor decreased and approached saturation. Further addition of cysteine to the buffer caused the voltage across the sensor to decrease further. With an increase in cysteine concentrations from 10 to 400 µM, the voltage across the sensor decreased from 30 to 8 mV, respectively under a 2-N load (Fig. 5G), consistent with the *I–V* characteristics of the sensor in the presence of different cysteine concentrations (Fig. 2C). Typical MSM device behaviour was observed. With increased cysteine concentrations, the resistance of the device (sensor) decreased due to an increase in charge carrier density (electrons) and thus the voltage across the sensor decreased. This potential drop across the sensor showed a monotonic relationship with cysteine concentrations (inset, Fig. 5G). The non-linearity of the self-powered cysteine sensor was attributed to the PNG's instantaneous voltage, as there is a small time lag between

the PNG's output and continuous cysteine sensor response. However, the cysteine sensor itself has a linear response (Fig. 2D).

4. Conclusions

We report for the first time the facile, direct detection of cysteine using functionalized BT NPs. Amine-functionalised BT NPs suspended in an agarose matrix were used for cysteine detection based on the change in surface charge properties of the composite film. The novel composite was also investigated for harvesting energy, leading to the development of a self-powered device. The agarose biopolymer and biocompatible BT NPs were used for sensing as well as for energy harvesting resulting in green chemistry. The as-fabricated sensor showed good selectivity, reproducibility, low cost, and detection limits down to ~ 10 μM. The study may further lead to the realization of functionalized BT NPs in theranostic applications and novel piezoelectric-biosensing devices.

Conflict of interest

The authors declare no competing financial interests.

Acknowledgements

This work was supported by the National Research Foundation of Korea (NRF) funded by the Korea Government GRANT (2016R1A2B2013831).

Appendix A. Supplementary data

Supporting information associated with this article can be found in the online version.

References

Alluri, N.R., Saravanakumar, B., Kim, S.J., 2015. ACS Appl. Mater. Interfaces 7, 9831–9840.

Carroll, M.L.C. and K.S., 2012. The Chemistry of Thiol Oxidation and Detection. Oxidative Stress Redox Regul.

Coates, J., Ed, R.A.M., Coates, J., 2000. Encycl. Anal. Chem. 10815–10837.

Culic-viskota, J., 2012. Synthesis and Functionalization of Second Harmonic Generation Nanocrystals and Their Application in Biological Imaging 2012.

Ĉulić-Viskota, J., Dempsey, W.P., Fraser, S.E., Pantazis, P., 2012. Nat. Protoc. 7, 1618–1633.

FarrokhTakin, E., Ciofani, G., Puleo, G.L., de Vito, G., Filippeschi, C., Mazzolai, B., Piazza, V., Mattoli, V., 2013. Int. J. Nanomedicine 8, 2319–31.

Freile-Pelegrin, Y., Madera-Santana, T., Robledo, D., Veleva, L., Quintana, P., Azamar, J.A., 2007. Polym. Degrad. Stab. 92, 244–252.

Gong, Q., Zhang, R., Yang, J., Huang, Z., Li, N., Zhao, N., Tang, B.Z., 2015. J. Mater. Chem. C 3, 8397–8402.

Han, C., Xu, K., Liu, Q., Liu, X., Li, J., 2014. Sensors Actuators, B Chem. 202, 574–582.

Hayashi, H., Nakamura, T., Ebina, T., 2013. J. Phys. Chem. Solids 74, 957–962.

Horger, K.S., Estes, D.J., Capone, R., Mayer, M., 2009. J. Am. Chem. Soc., 131 (5), 1810–1819.

Hsieh, C.-L., Grange, R., Pu, Y., Psaltis, D., 2010. Biomaterials 31, 2272–2277.

Hwang, G., Kim, J.-M., Hong, D., Kim, C.-K., Choi, N.-S., Lee, S.-Y., Park, S., 2016. Green Chem. 14–19.

Johnson, F., Levanon, H., Norris, J.R., Johnson, F., 1970. Chemical Reviews. Nature 227,

419–419.

Jung, H.S., Han, J.H., Pradhan, T., Kim, S., Lee, S.W., Sessler, J.L., Kim, T.W., Kang, C., Kim, J.S., 2012a. Biomaterials 33, 945–953.

Jung, H.S., Pradhan, T., Han, J.H., Heo, K.J., Lee, J.H., Kang, C., Kim, J.S., 2012b. Biomaterials 33, 8495–8502.

Kaniowska, E., Chwatko, G., Głowacki, R., Kubalczyk, P., Bald, E., 1998. J. Chromatogr. A 798, 27–35.

Lou, X., Zhao, Z., Hong, Y., Dong, C., Min, X., Zhuang, Y., Xu, X., Jia, Y., Xia, F., Tang, B.Z., 2014. Nanoscale 6, 14691–14696.

Nekrassova, O., Lawrence, N.S., Compton, R.G., 2003. Talanta 60, 1085–1095.

Park, S.J., Song, H.S., Kwon, O.S., Chung, J.H., Lee, S.H., An, J.H., Ahn, S.R., Lee, J.E., Yoon, H., Park, T.H., Jang, J., 2014. Sci. Rep. 4, 4342.

Park, K. Il, Lee, M., Liu, Y., Moon, S., Hwang, G.T., Zhu, G., Kim, J.E., Kim, S.O., Kim, D.K., Wang, Z.L., Lee, K.J., 2012. Adv. Mater. 24, 2999–3004.

Refsum, H., Ueland, P.M., Kvinnsland, S., 1986. Cancer Res 46, 5385–5391.

Santhiago, M., Lima, P.R., Santos, W. de J.R., Kubota, L.T., 2010. Sensors Actuators, B Chem. 146, 213–220.

Saravanakumar, B., Soyoon, S., Kim, S., 2014. ACS Appl. Mater. Interfaces 6, 13716–13723.

Selvarajan, S., Alluri, N.R., Chandrasekhar, A., Kim, S.-J., 2016. Sensors Actuators B Chem. 234, 395–403.

Sun, J., Yang, F., Zhao, D., Chen, C., Yang, X., 2015. ACS Appl. Mater. Interfaces 7, 6860–6866.

Sun, Z., Han, C., Song, M., Wen, L., Tian, D., Li, H., Jiang, L., 2014. Adv. Mater. 26, 455–460.

Thoniyot, P., Tan, M.J., Karim, A.A., Young, D.J., Loh, X.J., 2015. Adv. Sci. 2.

Wang, L., Zhang, Y., Li, X., Xie, Y., He, J., Yu, J., Song, Y., 2015. Sci. Rep. 5, 14341.

Wang, Z., Zhang, R., Ma, Y., Zheng, L., Peng, A., Fu, H., Yao, J., 2010. J. Mater. Chem. 20, 1107.

Xia, F., Ge, H., Hou, Y., Sun, T., Chen, L., Zhang, G., Jiang, L., 2007. Adv. Mater. 19, 2520–2524.

Yang, C., Wang, X., Shen, L., Deng, W., Liu, H., Ge, S., Yan, M., Song, X., 2016. Biosens. Bioelectron. 80, 17–23.

Yu, R., Pan, C., Chen, J., Zhu, G., Wang, Z.L., 2013. Adv. Funct. Mater. 23, 5868–5874.

Zhang, M., Yu, M., Li, F., Zhu, M., Li, M., Gao, Y., Li, L., Liu, Z., Zhang, J., Zhang, D., Yi, T., Huang, C., 2007. J. Am. Chem. Soc. 129, 10322–10323.

Zhang, R., Yu, X., Ye, Z., Wang, G., Zhang, W., Yuan, J., 2010. Inorg. Chem. 49, 7898–7903.

Figure captions

Figure 1. Schematic diagram and structural characterisation. Schematic illustration of the as-fabricated (A) cysteine sensor and (B) $BaTiO_3$/agarose (BT/Ag) nanogenerator. (C) Fourier-transform infrared spectra of BT nanoparticles (NPs) before and after NH_2 functionalization. (D) X-ray diffraction spectra for pristine BT NPs, BT-NH_2 NPs, Ag/BT-NH_2 film, and pristine Ag. Scanning electron microscopy images of (E) pristine Ag film, (F) Ag/BT-NH_2 film (inset shows BT-NH_2 NPs of size ≤ 200 nm), and (G) a cross-sectional view of Ag/BT-NH_2 film with a film thickness of ~50 µm.

Figure 2. Cysteine detection using a current–voltage (*I–V*) technique. (A) Two-dimensional (2D) graph depicting the performance of a cysteine sensor in the absence and presence of ultraviolet (UV) light (365 nm). (B) Three-dimensional (3D) graphical representation of the cysteine sensor's relative change in current ($I-I_0/I_0$) with respect to BT-NH_2 NP and cysteine concentrations. (C) *I–V* curves of Ag/BT-NH_2 film-based cysteine sensor (0.2% w/v) in response to various cysteine concentrations (10–1000 µM). (D) Normalized current value ($|I-I_0|$) of the sensor at −4 V for different cysteine concentrations (10–1000 µM; calibration plot obtained from *I–V* curves).

Figure 3. Schematic representation. (A) Proposed mechanism of cysteine detection (B) Reaction scheme for amine functionalization of BT NPs using (3-aminopropyl) triethoxysilane (APTES, a silane coupling agent).

Figure 4. Real sample analysis and interference studies. (A) *I–V* response of the Ag/BT-NH_2 film-based cysteine sensor in the presence of a urine sample spiked with different cysteine

concentrations (10–500 µM). (B) Normalized current value ($|I-I_0|$) of the sensor at −4 V in the presence of different concentrations of cysteine-spiked urine sample (10–500 µM; calibration plot obtained from *I*–*V* curves). (C) Current change ratio of cysteine sensor measured at −4 V in 0.1 M PBS (pH 7) with the addition of 1 mM Cys, His, Gln, AA, and UA.

Figure 5. Self-powered cysteine sensor. (A) Output voltage and current of BT/Ag nanogenerator as a function of different concentrations of BT NPs (% w/v) at a mechanical load of 2 N. (B) Open circuit voltage (V_{oc}) and (C) short-circuit current (I_{sc}) of BT/Ag nanogenerator (0.4% w/v) at 2 N. (D) Demonstration of commercial green light-emitting diodes (LEDs) lit using the piezoelectric potential generated. (E) Stable output voltage of the nanogenerator (under a load of 2 N) for a period of 1000 s with no degradation. (F) Output voltage of the nanogenerator (NG) and self-powered cysteine sensor (NG/cysteine sensor) under a load of 2 N. (G) The open-circuit potential drop across the sensor as a function of different cysteine concentrations (10^{-2} mM to 4×10^{-1} mM) at 2 N (inset shows the calibration plot where the potential drop across the sensor has a monotonic functional relationship with the cysteine concentration).

Graphical abstract

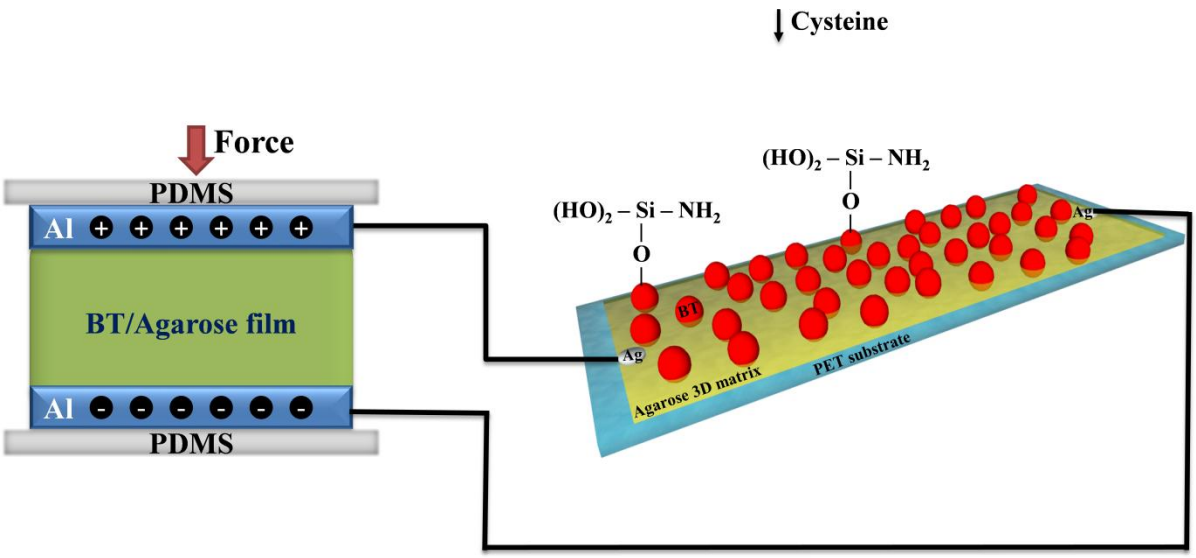

Highlights

- Facile and direct detection of cysteine through I-V technique has been reported for the first time.

- Functionalized $BaTiO_3$ NPs suspended in three dimensional agarose matrix was employed for self-powered cysteine biosensing system.
- Biocompatible $BaTiO_3$ NPs and agarose biopolymer paves way for green chemistry.
- The reported sensor has good selectivity and detection limits down to 10 µM (3s/m)
- The findings may further lead to novel piezoelectric-biosensing devices.